Electrochimica Acta 284 (2018) 119–127

Contents lists available at ScienceDirect

Electrochimica Acta

journal homepage: www.elsevier.com/locate/electacta

Nanocomposites CoPt-x/Diatomite-C as oxygen reversible electrocatalysts for zinc-air batteries: Diatomite boosted the catalytic activity and durability

Kai Wang [a], Zhenghua Tang [a, b, *], Wen Wu [a], Pinxian Xi [c], Dong Liu [d], Zhaoqing Ding [a], Xiaoning Chen [a], Xiao Wu [a], Shaowei Chen [a, e]

[a] Guangzhou Key Laboratory for Surface Chemistry of Energy Materials and New Energy Research Institute, School of Environment and Energy, South China University of Technology, Guangzhou Higher Education Mega Centre, Guangzhou, 510006, China
[b] Guangdong Provincial Key Laboratory of Atmospheric Environment and Pollution Control, Guangdong Provincial Engineering and Technology Research Center for Environmental Risk Prevention and Emergency Disposal, South China University of Technology, Guangzhou Higher Education Mega Centre, Guangzhou, 510006, China
[c] State Key Laboratory of Applied Organic Chemistry, Key Laboratory of Nonferrous Metal Chemistry and Resources Utilization of Gansu Province, College of Chemistry and Chemical Engineering, Lanzhou University, Lanzhou, 730000, China
[d] CAS Key Laboratory of Mineralogy and Metallogeny, Guangdong Provincial Key Laboratory of Mineral Physics and Materials, Guangzhou Institute of Geochemistry, Chinese Academy of Sciences, Wushan, Guangzhou, 510640, China
[e] Department of Chemistry and Biochemistry, University of California, 1156 High Street, Santa Cruz, CA 95064, United States

ARTICLE INFO

Article history:
Received 20 May 2018
Received in revised form
26 June 2018
Accepted 21 July 2018
Available online 24 July 2018

Keywords:
Diatomite
Bi-functional electrocatalysts
Oxygen reduction reaction
Oxygen evolution reaction
Zn-air battery

ABSTRACT

The exploration of oxygen reversible electrocatalysts to boost oxygen reduction reaction and oxygen evolution reaction is critical for the development of high-performance aqueous Zn-air batteries. Since diatomite with porous structure can adsorb metal ions in aqueous solution, herein, we prepare the nanocomposite CoPt-x/Diatomite-C for both oxygen reduction and evolution reactions, and diatomite is found significantly promotes the electrocatalytic activity and durability. With the presence of diatomite, CoPt-1/Diatomite-C shows a lower Tafel slope (63 mV dec^{-1} at high potential range), larger diffusion-limited current density (4.94 mA cm^{-2}) and superior durability for ORR. Particularly, the specific and mass activities of CoPt-1/Diatomite-C for ORR are 0.74 mA cm^{-2} and 286 mA mg^{-1}, respectively, which are 2.5 and 3.0 times higher than that of CoPt-1/C without diatomite; For OER, the overpotential of CoPt-9/Diatomite-C decreases nearly 30 mV at 10 mA cm^{-2}, while the Tafel slope also reduces 16 mV dec^{-1} versus CoPt-9/C catalyst. Moreover, a rechargeable Zn-air battery with these composites as air-cathode is self-assembled, and diatomite boosts the battery performance with desirable properties. CoPt-9/Diatomite-C displays the optimal performance, with a power density of 140 mW cm^{-2}, a specific capacity of 616 mA h g^{-1} at 10 mA cm^{-2} and an exceedingly robust cycling life. This work provides a viable and cost-effective strategy for fabricating oxygen reversible electrocatalysts for metal-air battery applications.

1. Introduction

Rechargeable zinc-air batteries are gaining increasing attentions in energy storage and conversion thanks to their high theoretical energy density, low cost and safety [1–3]. However, the large-scale commercialization of rechargeable zinc-air batteries has been significantly hindered by the sluggish reaction kinetics of both oxygen reduction reaction (ORR) and oxygen evolution reaction (OER) occurring at the cathode [4–8]. Therefore, developing more efficient and durable oxygen reversible electrocatalysts as air-cathode for zinc-air batteries are highly desirable [9,10].

Currently, Pt-based materials have been considered as the benchmark ORR catalysts while Ru/Ir based materials possess the best OER activities [11–13]. However, all these noble-metal-based

* Corresponding author. Guangzhou Key Laboratory for Surface Chemistry of Energy Materials and New Energy Research Institute, School of Environment and Energy, South China University of Technology, Guangzhou Higher Education Mega Centre, Guangzhou, 510006, China.
E-mail address: zhht@scut.edu.cn (Z. Tang).

https://doi.org/10.1016/j.electacta.2018.07.154
0013-4686/

materials are suffering from limited availability resulted high costs as well as poor stability for practical applications. To reduce the cost and acquire enhanced activity and stability, one effective strategy is to alloy the noble metals with 3d transitional metals [14]. For instance, a variety of Pt-M (M = Fe [15,16], Co [17,18], Ni [19,20] and other transition metals) alloys with different structures and various morphologies have demonstrated superior catalytic activity toward ORR than Pt. On the other hand, transition metal oxides, hydroxides and complexes have demonstrated great potentials in catalyzing OER to serve as alternatives for Ir or Ru based materials [21–25]. To realize real-world applications of the catalyst for rechargeable zinc-air battery, it is essential to integrate both ORR and OER catalytic activity into one sample [26]. The so-called "Two-in-one" strategy requires the rational design, which not only can achieve optimized performance in both reactions, but also be able to develop a facile and cost-effective approach for fabrication [27]. Coupling PtM alloys with transitional metal oxides or complexes to fabricate hybrid materials can be a viable strategy and have shown great promises for catalyzing both ORR and OER and/or for further zinc-air battery applications. Through a laser ablation synthesis, PtCo nanoalloys embedded in CoO_x matrices have been prepared as bifunctional electrocatalysts for ORR and OER by Mukherjee group, and a combined overpotential of 756 mV vs. RHE for the sample of PtCo-3 NC was achieved [28]. Goodenough group developed a robust Fe_3Mo_3C supported IrMn clusters as bifunctional air-electrode, which could enable Zn—air batteries to achieve long-term cycling performance over 200 h with high efficiency [29]. In addition, porous metallic nickel-iron nitride (Ni_3FeN) supporting ordered Fe_3Pt intermetallic nanoalloy was also prepared by this group as advanced bifunctional electrocatalysts for zinc-air battery, and a long-term cycling performance of over 480 h at 10 mA cm^{-2} was recorded [30].

Despite these progresses on bi-functional electrocatalysts for ORR and OER, the activity and durability for the two reactions are far from satisfaction. Furthermore, the preparation of these hybrid materials was also tedious, sophisticated and time-consuming hence not cost-effective. Herein, we developed a new strategy for preparing highly efficient electrocatalysts toward both ORR and OER for zinc-air batteries. As PtM alloys have already demonstrated excellent activity toward ORR, and metal oxides showed good OER performance, instead of simply combining PtM alloys with transitional metal oxides, we developed a strategy to integrate CoPt nanoparticles with SiO_2 as dual functional electrocatalysts for both ORR and OER, where SiO_2 are from widely accessible natural diatomite (DTM). Note that, diatomite (DTM) is a near pure sedimentary deposit consisting almost entirely of silica (SiO_2). Known as diatomaceous earth, DTM is the naturally occurring fossilized remains of diatoms, which are ubiquitous in nature hence extremely cheap [31,32]. Furthermore, DTM possesses porous structure which not only can adsorb metal ions, but also is favourable for electrocatalytic reaction.

In this study, we prepared the composite CoPt-x/DTM-C via reducing the Pt^{4+} and Co^{2+} ions that were co-adsorbed into the DTM in ethylene glycol solution. TEM analysis demonstrated that CoPt nanoparticles were well-dispersed on the surface of the DTM. The nanocomposite catalyst exhibited excellent performance for both ORR and OER, and we found that DTM significantly promoted the electrocatalytic activity and long-term durability. With the presence of the DTM, the catalysts showed lower Tafel slope, higher diffusion-limited current and significantly enhanced durability. The specific and mass activities of CoPt-1/DTM-C for ORR are 0.74 mA cm^{-2} and 286 mA mg^{-1} (at 0.9 V vs. RHE), which are 2.5 and 3.0 times higher than that of CoPt-1/C catalyst; the overpotential of CoPt-9/DTM-C for OER decreased nearly 30 mV versus CoPt-9/C catalyst. In the rechargeable Zn-air battery applications, CoPt-9/DTM-C displayed superior performance than the sample without DTM and the other samples, with a power density of 140 mW cm^{-2}, a specific capacity of 616 mAh g^{-1} at the current density of 10 mA cm^{-2} and an exceedingly robust cycling life.

2. Experimental section

2.1. Materials

Diatomite was received from the Guangzhou Institute of Geochemistry, Chinese Academy of Science, ethylene glycol (EG, 99.9%, Tianjin Fuchen Chemical Regents), hydrochloric acid (HCl, 37%, Tianjin Damao Chemical Regents), cobalt chloride hexahydrate ($CoCl_2 \cdot 6H_2O$, 97%, Tianjin Fuchen Chemical Regents), chloroplatinic acid hexahydrate ($H_2PtCl_6 \cdot 6H_2O$, 99.9%, Energy Chemicals, Shanghai, China), commercial Pt/C (20 wt%, Alfa Aesar). Water was supplied by a Barnstead Nanopure Water System (18.3 MΩ cm). All the chemicals were used as received without further purification.

2.2. Preparation of nanocomposite electrocatalysts

All the CoPt-x/DTM-C (x equaling to the molar ratio of Co-to-Pt) samples were prepared via a conventional ethylene glycol (EG) reduction method. Take CoPt-1/DTM-C as an example, and the detailed procedure is described below: DTM was first immersed into the HCl solution (3 M, 40 mL) under stirring overnight, then washed with de-ionized water until the pH of the filtrate reached ~7. The filter cake was dried at 40 °C under vacuum overnight. Subsequently, $H_2PtCl_6 \cdot 6H_2O$ (0.15 mmol) and $CoCl_2 \cdot 6H_2O$ (0.15 mmol) were dissolved in EG (20 mL) with sonication for 15 min, the above obtained solid (76 mg) was added to the above solution under vigorous stirring at room temperature for 4 h to ensure the Pt^{4+} and Co^{2+} ions were completely adsorbed. The mixture was then heated to 160 °C for 6 h. After that, it was cooled down to 40 °C, and XC-72 (76 mg) was added. The solution was kept 40 °C for 4 h under magnetic stirring. The whole process was under protection of nitrogen atmosphere. Afterward, the sample was separated by centrifugation, washed with de-ionized water several times, and dried at 40 °C under vacuum for 12 h. The synthesis of CoPt-3/DTM-C, CoPt-9/DTM-C was in the same manner with that of CoPt-1/DTM-C, except the amount of $CoCl_2 \cdot 6H_2O$ was changed into 0.45 mmol and 1.35 mmol, respectively, whereas for Co/DTM-C, 1.85 mmol $CoCl_2 \cdot 6H_2O$ and no $H_2PtCl_6 \cdot 6H_2O$ were added. Other than that, the samples of CoPt-x/C and Co-x/C were synthesized by following the procedure of CoPt-x/DTM-C and Co/DTM-C but without the addition of DTM. The weight percentage of platinum in the CoPt-x/DTM-C series and CoPt-x/C series are compiled in Table S1.

2.3. Characterizations

X-ray photoelectron spectroscopic (XPS) measurements were performed on a Thermo Escalab 250Xi instrument. Powder X-ray diffraction (XRD) patterns were recorded with a Bruker D8-Advance diffractometer using Cu K_α radiation. Transmission electron microscopic (TEM) measurements were carried out on high-resolution transmission electron microscope (JEOL-JEM-2010) with an acceleration voltage of 200 kV. Barrett-Emmett-Teller (BET) surface areas of the catalysts were measured by a Quantachrome Autosorb-iQ2 instrument with N_2 adsorption at 77 K using the Barret-Joyner-Halenda (BJH) method.

2.4. Electrochemical measurements

The electrochemical experiments were performed using a CHI

750E electrochemical workstation (CH Instruments, Chenhua Co Ltd., China) in 0.1 M or 1 M KOH aqueous solution at room temperature. A conventional three-electrode cell, comprising of an Ag/AgCl (3 M KCl) as the reference electrode, a glassy carbon rotating ring-disk electrode (RRDE, Pine instrument company, LLC) with diameter of 5 mm as the working electrode and a platinum plate as the counter electrode. The catalyst ink was prepared as follows: 2 mg catalyst was dispersed ultrasonically in 1 mL nafion/ethanol (1.0% nafion) formed a homogeneous suspension, and the concentration of metal was 0.4 mg mL^{-1}. 20 μL suspension was then dropcast onto the surface of the polished glassy carbon electrode, and dried at room temperature. The loading amount of metal was calculated to be 40.8 μg cm^{-2}. Prior to each measurement, the solution was purged with high-purity N_2 or O_2 gas for at least 30 min. The electrochemically active surface areas (ECSAs) of the catalysts were performed by integrating the hydrogen adsorption charge on the cyclic voltammograms (CVs) at the scan rate of 10 mV s^{-1} at room temperature in N_2-saturated 0.1 M $HClO_4$ aqueous solution. Linear sweep voltammograms (LSVs) were obtained at a sweep rate of 10 mV s^{-1} in N_2 or O_2-saturated 0.1 M KOH aqueous solution at various rotation rates (400–2500 rpm). The Ag/AgCl electrode was calibrated with a reversible hydrogen electrode (RHE), $E_{RHE} = E_{Ag/AgCl} + 0.196\ (V) + 0.0591^{*}(pH)$.

2.5. Battery test

The Zn-air battery was self-designed and fabricated by using the zinc plate as the anode, the catalyst loaded on carbon cloth as the air-cathode and 6 M KOH plus 0.2 M ZnAc as the electrolyte. All Zn-air battery tests were carried out by the CHI-440 electrochemical workstation (CH Instruments, Chenhua Co Ltd., China) at ambient conditions. The detailed preparation process can be found in supplementary materials.

3. Results and discussions

3.1. TEM image and XRD patterns of the CoPt-x/DTM-C composites

Upon the preparation of the composite, the pore structure and specific surface area of the CoPt-1/DTM-C, CoPt-1/C and diatomite samples were examined by N_2 adsorption–desorption isotherms. As shown in Fig. S1, all of the N_2 adsorption-desorption isotherms exhibited a characteristic feature as type II isotherms with H3 type hysteresis loops. The hysteresis can be associated with the filling and emptying of the mesopores by capillary condensation, suggesting the existence of mesopores [33]. In addition, a sharp increase in the N_2 adsorption quantity near the relative pressure of 1 implies the existence of macropores [33]. Such feature suggests the both macropores and mesopores co-exist in those materials. The N_2 adsorption-desorption isotherms and the corresponding pore size distribution show DTM possesses hierarchical porous structure. Nevertheless, DTM contains less micropores and mesopores, resulting relatively smaller specific surface area than most porous carbon materials [33]. XC-72 has a larger specific surface area, once it was added in, the surface area of the composites (CoPt-x/DTM-C) was significantly enhanced. Based on the Brunauer-Emmett-Teller (BET) curves, the BET surface area of CoPt-1/DTM-C, CoPt-1/C and DTM were calculated as 88 $m^2\,g^{-1}$, 160 $m^2\,g^{-1}$ and 13 $m^2\,g^{-1}$, respectively.

Then, the surface microstructure and morphology of the CoPt-x/DTM-C samples were examined by TEM. Fig. 1A–C presents the representative TEM, HR-TEM image of the CoPt-1/DTM-C sample. As shown in Fig. 1A, CoPt nanoparticles were well dispersed on the DTM-C support, and the diameter was roughly about 4–5 nm. Fig. 1B clearly revealed that the alloyed nanoparticles were confined in the support. Note that Pt^{4+} and Co^{2+} ions were first adsorbed and reduced in the pores of the DTM, and then a layer of XC-72 was added to cover the nanoparticles. The CoPt nanoparticles were well protected and such structure is probably favourable for enhancing the electrocatalytic activity and durability for ORR and OER. The representative TEM and HR-TEM images of the CoPt-1/C are shown in Fig. S2, while the typical TEM and HR-TEM images of the CoPt-9/DTM-C and CoPt-9/C samples can be found in Fig. S3. As shown in insert graphs of Fig. 1B and Fig. S2b, the average diameter of CoPt nanoparticles was estimated to be 3.20 ± 0.86 nm for CoPt-1/DTM-C and 3.80 ± 0.96 nm for CoPt-1/C. The insert graphs of Fig. S3b and e indicate that the average diameter of CoPt nanoparticles was 3.40 ± 1.17 nm and 3.90 ± 1.97 nm for CoPt-9/DTM-C and CoPt-9/C, respectively. It can be noted that, with the presence of DTM, relatively smaller CoPt nanoparticles can be acquired. From the HR-TEM images in Fig. 1C, well-defined lattice fringes of the CoPt-1/DTM-C sample can be recognized. The inter-planar spacings are 2.09 Å and 2.30 Å, which correspond to the (111) and (200) lattice plane of the face-centered-cubic (fcc) CoPt nanoparticles, and amorphous SiO_2 and XC-72 show the disordered lattice fringes.

The crystal structure of the composite was next investigated by XRD measurements. As shown in Fig. 1D, the presence of the (111), (200), (220) planes from Pt indicated that CoPt nanoparticles with fcc structures were probably obtained. Interestingly, compared with the standard Pt (JPCDS No. 01-1190), the diffraction peaks of Pt were shifted to higher degrees for both CoPt-1/DTM-C and CoPt-1/C samples. Previous studies have shown that these shifts were probably attributed to the decrease of the lattice distance upon the formation of CoPt alloyed nanoparticles [34]. A broad diffraction peak at $2\theta = 22.1^{\circ}$ can be easily identified in Fig. 1D (a), which is classified as amorphous SiO_2 (JPCDS No. 29-0085). Compared with Fig. 1D (b), the peak from XC-72 became much less identifiable in Fig. 1D (a), which might be suppressed by the broad peak of amorphous SiO_2. In addition, Fig. S4 presents the XRD patterns of CoPt-9/DTM-C, and similar XRD feature can be observed.

3.2. XPS measurements

The surface chemical composition and valence state of CoPt-1/DTM-C and CoPt-1/C were subsequently explored by XPS measurements. As shown in Fig. 2a, the Pt 4f core-level spectra of CoPt-1/DTM-C displayed a pair of major peaks with the binding energies at 71.4 eV and 74.5 eV, which can be attributed to the Pt $4f_{7/2}$ and Pt $4f_{5/2}$ electrons, respectively. Compared with the CoPt-1/C sample without DTM, the binding energy of the Pt $4f_{5/2}$ electrons from the CoPt-1/DTM-C sample shifted negatively about 0.24 eV, indicating the Pt ions can be more easily reduced to form CoPt nanoparticles in the presence of DTM. The Pt 4f spectra can be de-convoluted into two doublets, which were attributed to Pt^{2+} (PtO and $Pt(OH)_2$) and Pt^0 (metallic Pt). Based on the integral area, the percentage of Pt^{2+} and Pt^0 can be determined as ~36% and ~64% in CoPt-1/C, while in CoPt-1/DTM-C, the percentage of Pt^{2+} and Pt^0 was ~28% and ~72%, respectively. One can see that, regardless of the presence of DTM, Pt^0 species dominate the above components, and higher relative intensity of Pt^0 was observed for the CoPt-1/DTM-C sample, which is probably favourable for ORR, as Pt^0 can offer more appropriate active site for ORR than Pt^{2+} [35,36]. As the binding energy change of the core-level is associated with the shift of its d-band center relative to Fermi level in the same direction [37], the decreasing of Pt4f binding energy in the CoPt-1/DTM-C sample indicates the downshift of its d-band center. According to the Hammer-Norskov model [38–40], such downshift can lower the state density at the Fermi Level and weaken the chemisorption bonds, leading to the reduced chemical adsorptions of OH_{ads} species on the surface and

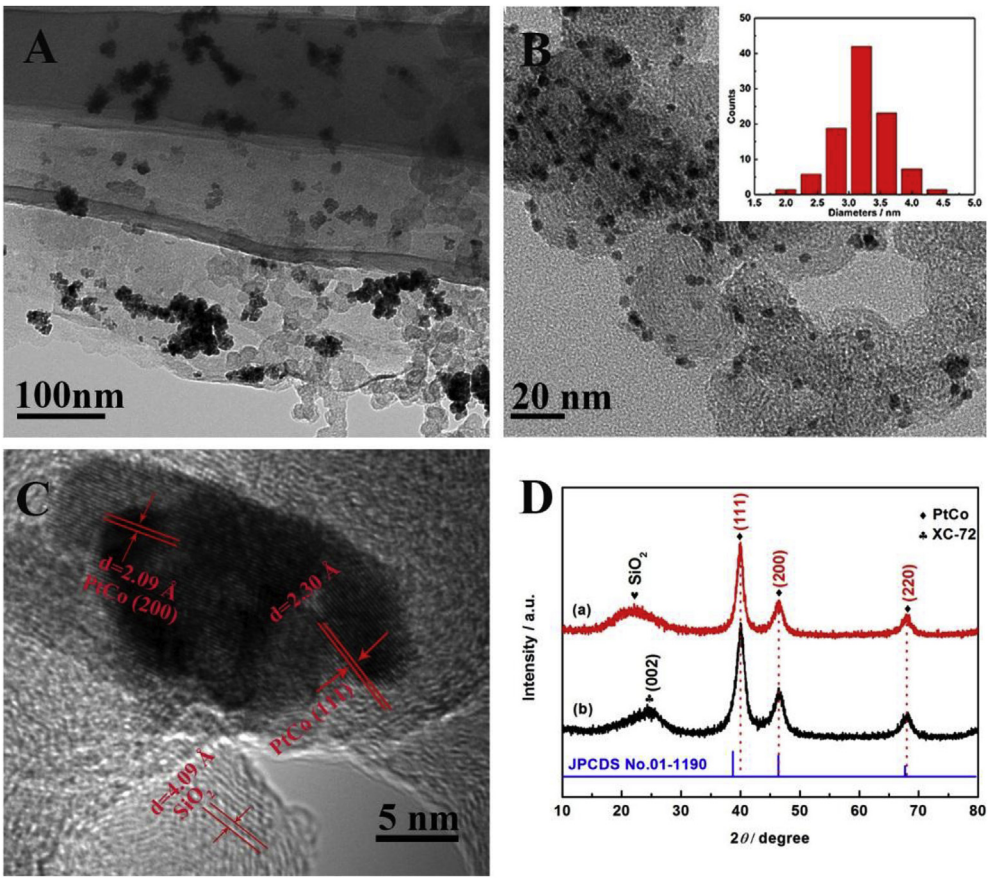

Fig. 1. The representative TEM images under different magnifications of CoPt-1/DTM-C (A–C), the inset in B is the size distribution histogram of the CoPt nanoparticles, and D is the XRD patterns of CoPt-1/DTM-C (a), CoPt-1/C (b).

generation of more active sites for ORR [41]. Furthermore, the core-level XPS spectra of the Co 2p electrons are presented in Fig. 2b. Compared with the CoPt-1/C sample, the binding energy of the Co $2p_{3/2}$ electrons in the CoPt-1/DTM-C sample exhibited a distinct increase about 1 eV, indicating DTM promotes the electron transfer from Co atoms to Pt atoms. Similar pattern can also be observed for the CoPt-9/DTM-C and CoPt-9/C samples (Fig. S5). From the above results, one can see that, DTM played an important role in modifying the surface electronic structure of the CoPt alloyed nanoparticles.

3.3. ORR/OER catalytic performance

The as-prepared nanocomposites of CoPt-x/DTM-C were then subjected to electrocatalytic tests toward ORR and OER. Fig. 3a presents the polarization curves for ORR, one can see that, with the increasing of Pt amount (x = Co/Pt, x from 9 to 1), both the onset potential and half-wave potential shifted more positively. The most positive potential was achieved on the sample of CoPt-1/DTM-C. It is worth noting that, without Co, the sample of Pt/DTM-C still displayed excellent activity, however, its onset potential was approximately 20 mV lower than that of CoPt-1/DTM-C. Meanwhile, from the polarization curves for OER in Fig. 3b, it can be noted that the overpotential decreased with the increasing of the Co/Pt ratio. The overpotential of CoPt-1/DTM-C and CoPt-3/DTM-C was approximately 460 mV (vs. RHE) and 430 mV (vs. RHE) at the current density of 10 mA cm^{-2}, respectively. CoPt-9/DTM-C exhibited the lowest overpotential of 380 mV (vs. RHE), which was about 20 mV lower than the sample of Co/DTM-C.

To further evaluate the role of DTM in the electrocatalytic process for ORR, we next performed a series of electrochemical characterizations. Fig. 4a displays the cyclic voltammograms recorded in both N_2-saturated and O_2-saturated 0.1 M KOH of the samples CoPt-1/C and CoPt-1/DTM-C. In N_2-saturated 0.1 M KOH solution, both samples displayed featureless redox properties, however, when switched into O_2-saturated 0.1 M KOH solution, CoPt-1/C and CoPt-1/DTM-C all displayed an obvious reduction peak at 0.85 V and 0.87 V (vs. RHE), indicating effective electrocatalytic activities toward ORR for both samples. The polarization curves (Fig. 4b) further revealed the onset potential and diffusion-limited current density of CoPt-1/C, CoPt-1/DTM-C and commercial Pt/C. The onset potential for CoPt-1/C, Pt/C, CoPt-1/DTM-C was 0.95 V, 0.97 V, and 0.99 V at the current density of 0.1 mA cm^{-2}, respectively, while the diffusion-limited current density was 4.76 mA cm^{-2}, 4.84 mA cm^{-2}, and 4.94 mA cm^{-2}, respectively. It can be noted that, CoPt-1/C possessed less positive onset potential and lower current density than commercial Pt/C, however, with the presence of DTM, CoPt-1/DTM-C exhibited more positive potential and larger diffusion-limited current density than Pt/C. Apparently, DTM promoted the ORR activity of the hybrid composite. Subsequently, Tafel-plots were fitted through the polarization curves in Fig. 4c to reveal the reaction kinetics. Similar features were obtained for the three catalysts. In fact, there are two linear regions at low and high overpotentials for the Tafel plots, which have been well documented in previous reports [42–44]. In the low overpotential range, the Tafel slopes were found at 77 mV dec^{-1}, 74 mV dec^{-1} and 63 mV dec^{-1} for CoPt-1/C, Pt/C and CoPt-1/DTM-C, respectively, suggesting the rate determining step in oxygen electroreduction is probably a

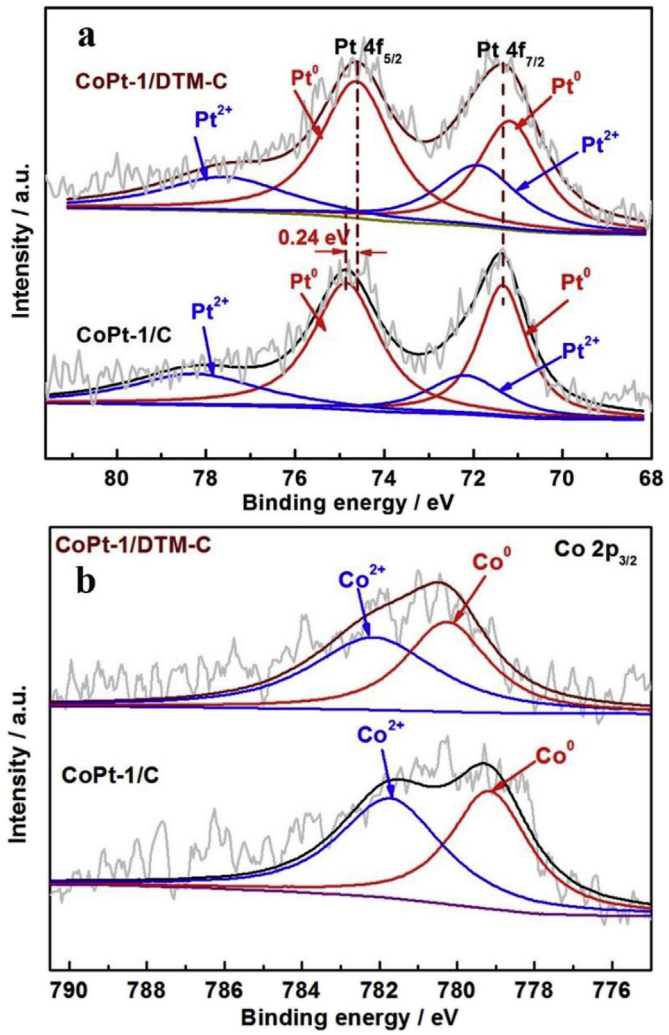

Fig. 2. The Pt 4f (a) and Co 2p (b) focus scan XPS spectra in the samples of CoPt-1/DTM-C and CoPt-1/C.

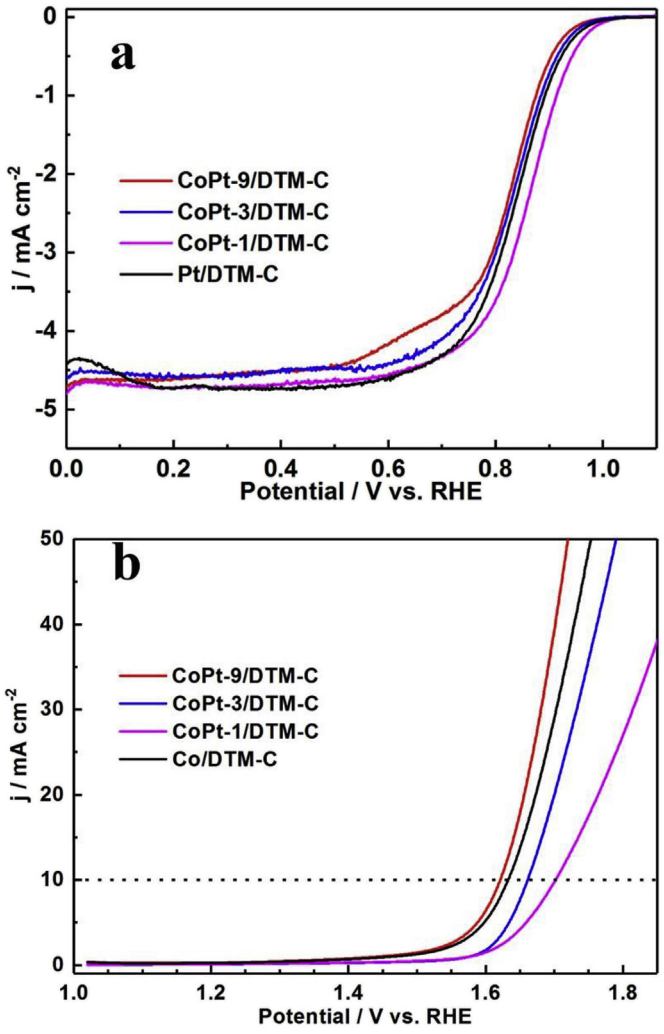

Fig. 3. The effect of cobaltic content as oxygen electrocatalyst in the presence of diatomite: (a) Linear sweep voltammograms for ORR in oxygen-saturated 0.1 M KOH, and (b) in nitrogen-saturated 1 M KOH for OER at the rotation rates of 1600 rpm.

pseudo two-electron transfer reaction [18]. While in the higher overpotential range, the slopes were 126 mV dec^{-1}, 121 mV dec^{-1} and 113 mV dec^{-1} for CoPt-1/C, Pt/C and CoPt-1/DTM-C, indicating that the reaction rate was dominated by the first electron transfer to oxygen molecule [12,42]. The comparison of the Tafel plots of the CoPt-x/DTM-C series for ORR can also be found in Fig. S6. One may notice that, with the presence of DTM, both the Tafel slopes at low or high overpotentials were reduced, which implies that DTM can facilitate the ORR kinetics.

The RRDE voltammetric curves with rotation rates varying from 400 rpm to 2500 rpm can be found in Fig. 4d, and the current density increased with the increasing of the rotation rate. The inset corresponding Koutecky-Levich (K-L) plots in Fig. 4d exhibited good linearity and consistent slopes in the potential range of +0.45 V to +0.75 V, indicating first-order reaction kinetics with regard of dissolved oxygen concentration in the solution.

Furthermore, the number (n) of electron transfer and yield of H_2O_2 (%) can be calculated by equations (1) and (2):

$$n = (4I_D)/(I_D + I_R/N) \quad (1)$$

$$H_2O_2\% = (200I_R/N)/(I_D + I_R/\mathrm{N}) \quad (2)$$

where I_D is the disk current, I_R is ring current, N is the current collection efficiency of the RRDE measurement (0.37). As shown in Fig. 4e, the electron transfer numbers of the CoPt-1/C, CoPt-1/DTM-C and Pt/C are 3.88–3.91, 3.81 to 4.0 and 3.94 to 3.96 in potential range from 0.2 V to 0.8 V, respectively. It suggests that the ORR reaction proceeds predominantly with the 4e pathway in 0.1 M KOH solution.

In addition, based on the CV curves in acidic electrolyte (Fig. S7), the electrochemically active surface area (ECSA) can be quantified and summarized in Table S2. By normalizing the kinetic current to the ECSA value and the Pt loading, the specific and mass activities of the CoPt-1/C, CoPt-1/DTM-C as well as Pt/C were calculated and shown in Fig. 4f. The specific activity of CoPt-1/C, CoPt-1/DTM-C, Pt/C was 0.29 mA cm^{-2}, 0.74 mA cm^{-2}, and 0.14 mA cm^{-2}, while the mass activity was 96 mA mg^{-1}, 286 mA mg^{-1} and 52.5 mA mg^{-1}, respectively. One can see that, DTM is an efficacious agent for promoting the electrocatalytic activity of ORR.

In addition, the OER activities of the nanocomposite catalysts were also evaluated by the LSVs in N_2-saturated 1 M KOH solution. As shown in Fig. 5a, with the current density of 10 mA cm^{-2}, the overpotential of CoPt-9/DTM-C, CoPt-9/C, Co/DTM-C and Co/C was 380 mV, 410 mV, 400 mV, and 420 mV, respectively. The overpotential of the CoPt-9/DTM-C was about 30 mV smaller than the

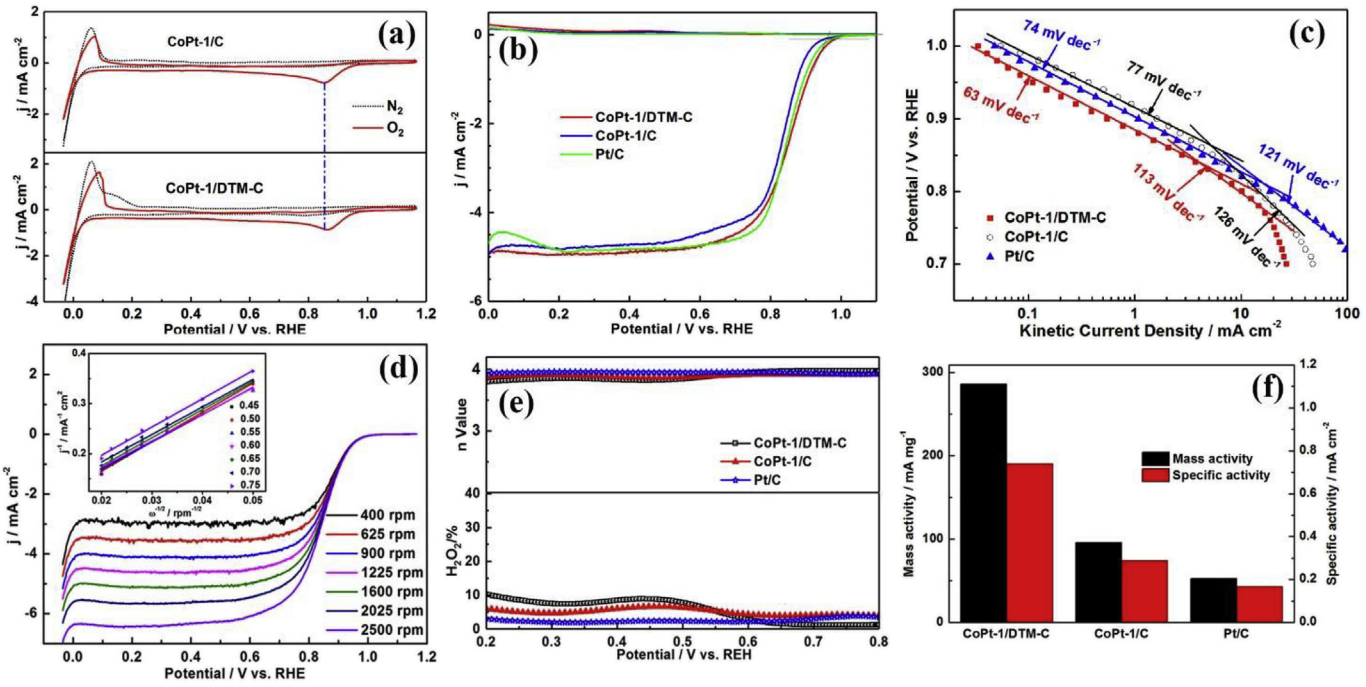

Fig. 4. (a) Cyclic voltammograms and (b) polarization curves for ORR, (c) Tafel plots of CoPt-1/DTM-C, CoPt-1/C and commercial Pt/C, (d) LSV curves for CoPt-1/DTM-C at the rotation rates of 400–2500 rpm (inset displays the corresponding K–L plots for CoPt-1/DTM-C at different electrode potentials), (e) Plots of H_2O_2 yield and number of electron transfer of a glassy carbon electrode modified with CoPt-1/DTM-C, CoPt-1/C and Pt/C in O_2-saturated 0.1 M KOH solution, (f) The comparison of mass activity and specific activity of CoPt-1/DTM-C and CoPt-1/C for ORR at 0.9 V (vs. RHE). All measurements were conducted at a metal loading of 40.8 μg cm^{-2} in an O_2-saturated 0.1 M KOH aqueous solution at a potential sweep rate of 10 mV s^{-1}.

CoPt-9/C, while compared with Co/C, the overpotential of Co/DTM-C also decreased approximately 20 mV at the current density of 10 mA cm^{-2}. DTM significantly reduced the overpotential and promoted the OER activity. Tafel plots were then fitted through the corresponding LSV curves. As presented in Fig. 5b, the Tafel slope of CoPt-9/DTM-C was 120 mV dec^{-1}, much lower than that of Co/C, Co/DTM-C, and CoPt-9/C. The results agree well with the polarization curves of the OER, further confirming that the presence of DTM was favourable for the OER catalytic kinetics. The comparison of the Tafel plots of the CoPt-x/DTM-C series for OER can be found in Fig. S8.

Note that, with the presence of DTM, either the ORR activity of the CoPt-1/DTM-C or the OER activity of CoPt-9/DTM-C was superior than recently reported CoPt nanoparticles based electrocatalysts. For instance, Mukerjee group prepared carbon-supported PtCo catalysts by the micro-emulsion method, but the mass activity and specific activity for ORR were only 154 mA/mg$_{Pt}$ and 0.58 mA/cm^2 [45]. Wang et al. reported that carbon supported Pt-Co nanoparticles as electrocatalyst for ORR, and the kinetic current density and mass activity were 1.85 times higher than that of commercial Pt/C, while the mass activity of CoPt-1/DTM-C was 5.45 times of Pt/C in this study [46]. Recently, Hu et al. documented the PtCo/CoO$_x$ nanocomposites as bi-functional electrocatalysts for both ORR and OER through tandem laser ablation synthesis, and the overpotential of the PtCo-1 can be reduced to 386 mV at the current density of 10 mA cm^{-2} [28], which was slightly higher than the CoPt-9/DTM-C sample (380 mV). Therefore, although DTM is not the active ingredients for ORR and OER, it is a vital element for CoPt nanoparticles in forming more catalytically active sites.

There are several contributions that can account for the enhancement of the ORR and OER activities of the CoPt-x/DTM-C nanocomposite catalysts in the presence of DTM. First of all, hierarchical porous DTM can provide facile path for mass (O_2/OH^-) transfer, which can significantly facilitate the electrocatalytic kinetics [47]. Secondly, DTM can alter the local electrical field around the CoPt nanoparticles, which is attested by the XPS observations, and such phenomenon will promote the collaborative interactions of CoPt for ORR. At last, the synergistic effects between the CoPt nanoparticles and DTM-C support further promote the ORR and OER catalytic processes [28,48].

Subsequently, the durability of CoPt-1/C and CoPt-1/DTM-C were carried out by the chronoamperometric measurements at 0.5 V in O_2-saturated 0.1 M KOH solution for ORR first. Fig. 6a shows that the current density of CoPt-1/C decayed rapidly in the first 6,000 s, while during the following 6,000 s to 30,000 s, the decline of the current density gradually slowed down. In total, the current density of CoPt-1/C decayed 20%. In sharp contrast, CoPt-1/DTM-C catalyst retained 95.6% of the initial current density after 30,000 s of continuous operation, indicating that DTM could significantly enhance the durability of CoPt nanoparticles for ORR. Furthermore, the durability of the catalysts for OER was also performed by the chronoamperometric measurements at 1.6 V (RHE) in N_2-saturated 1.0 M KOH solution, as shown in Fig. 6b. After continuous operation of 8.3 h, the CoPt-9/C sample maintained 81% of its initial current, while the CoPt-9/DTM-C sample only degraded 9% (91% maintained) of its initial value. One can conclude that, DTM indeed protected the CoPt nanoparticles during the oxygenic reaction. The enhanced long-term stability with the presence of DTM is probably attributed to the following factors: First of all, with the introduction of DTM, the as-formed silica sheets can prevent the dissolution of CoPt nanoparticles and the diffusion of dissolved CoPt species [49]. Secondly, the migration and agglomeration of CoPt nanoparticles on the support can also be significantly inhibited by DTM which hold well-defined porous structure [50].

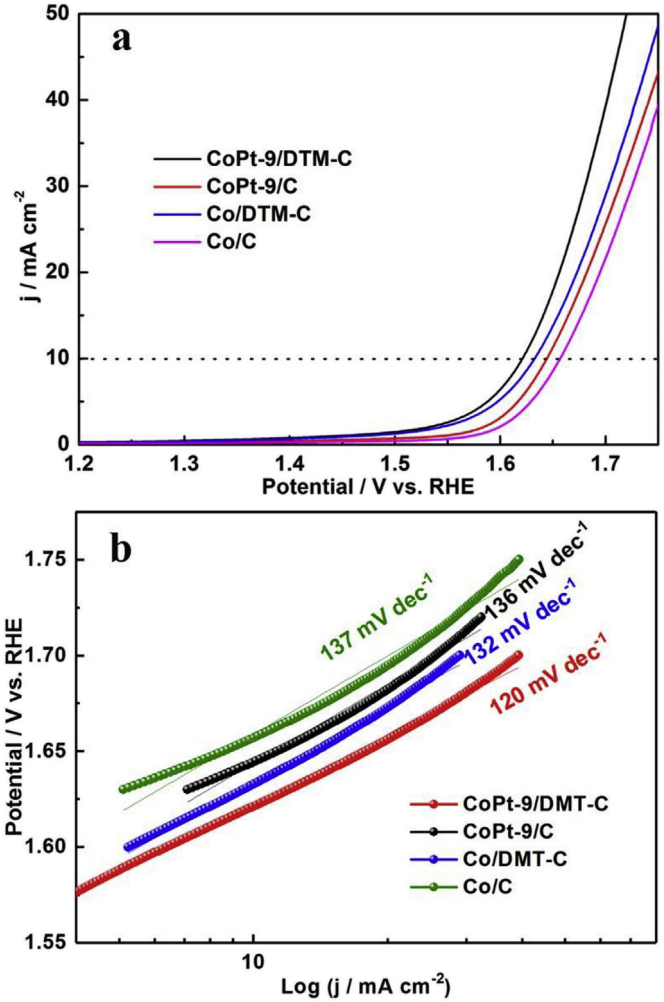

Fig. 5. (a) LSV curves measured in N_2-saturated 1 M KOH solution and (b) corresponding Tafel plots for OER (The scan rate is 10 mV s^{-1}).

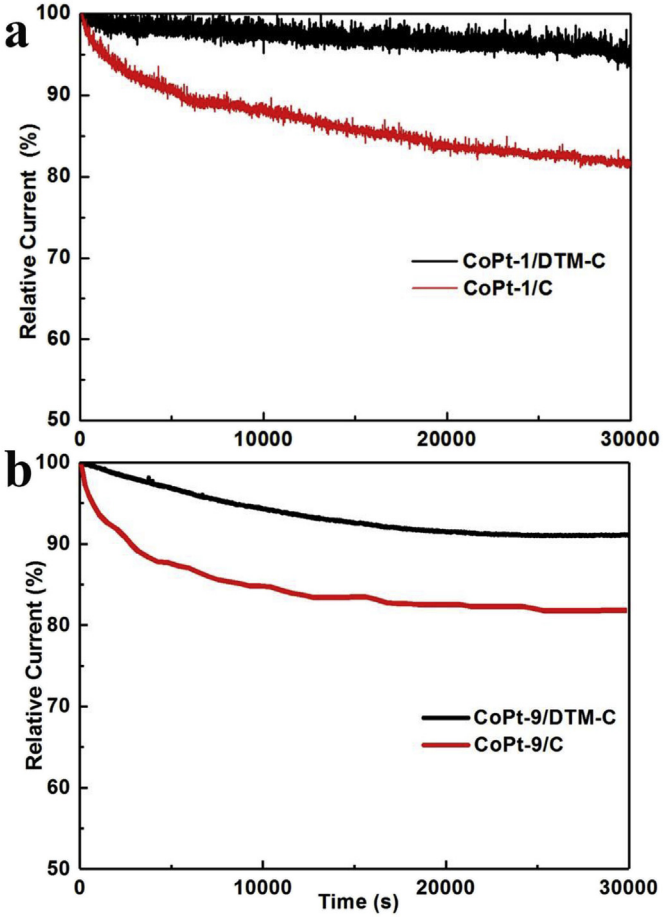

Fig. 6. Chronoamperometric responses in O_2-saturated 0.1 M KOH solution at 0.5 V for ORR (a), and in N_2-saturated 1 M KOH solution at 1.6 V for OER (b).

3.4. The Zn-air battery performance

Considering the excellent bifunctional oxygen catalytic performance of the nanocomposites, the feasibility of the composites in real battery conditions was then tested in a self-assembled rechargeable zinc-air battery [3]. Fig. 7a presents the schematics of the rechargeable zinc-air battery, where zinc plate was employed as anode and the catalysts were used as air-cathode. To ensure the reversible electrochemical reactions at anode, 0.2 M zinc acetate was dissolved in 6.0 M KOH as the electrolyte to evaluate the rechargeable performance of zinc-air batteries [10,51,52]. As shown in Fig. 7b, the open-circuit potential was 1.55 V and 1.44 V for CoPt-9/DTM-C and CoPt-9/C, respectively. The presence of DTM boosted the open circuit potential value. The discharge voltage curve and corresponding power density can be found in Fig. 7c, CoPt-9/DTM-C exhibited optimal maximal power density with a value of 140 mW cm^{-2}, higher than that of CoPt-9/C (123 mW cm^{-2}). The charge-discharge performance was then conducted with a constant current density of 2 mA cm^{-2} to evaluate the cycling life of the zinc-air battery. In Fig. 7d, the undulate charge voltage of CoPt-9/C can be observed, indicating the structure of the CoPt nanoparticles might be undermining at high voltages. The voltage gap and round-trip efficiency varied from 0.83 V to 1.19 V and 59%–45% for CoPt-9/C, yet the CoPt-9/DTM-C sustained an intriguing stability of 0.82–0.90 V and 60%–58% after galvanostatic charge–discharge test for continuous 8 h. Moreover, the galvanostatic discharge specific capacity was measured at the current density of 10 mA cm^{-2} and was normalized to the mass of lost zinc plate (Fig. 7e). The specific capacity of CoPt-9/DTM-C was calculated to be 616 mA h g^{-1}, much higher than that of CoPt-9/C (513 mA h g^{-1}). Finally, with CoPt-9/DTM-C supported on carbon cloth as the air-cathode of the two-series connected liquid Zn-air battery as practical power (Fig. 7f), a blue light-emitting diode (LED, ≈3.0 V) could glow about 12 h steadily at ambient conditions. The above findings suggest that DTM significantly boosted the performance in the zinc-air battery application of the supported CoPt nanoparticles.

4. Conclusions

In summary, composites based on CoPt-x/DTM-C have been prepared in a facile approach as bi-functional electrocatalysts toward both ORR and OER for rechargeable Zn-air battery applications. It was found that, hierarchical porous structure of DTM can significantly promote mass (O_2/OH^-) transfer, in addition, as a substrate it can alter the local electrical field around the CoPt nanoparticles. These characteristics affect the catalytic properties of CoPt-x/DTM-C. For ORR, with presence of DTM, CoPt-1/DTM-C exhibits a lower Tafel slope (63 mV dec^{-1}) and higher diffusion-limited current density (4.94 mA cm^{-2}). The specific and mass activities of CoPt-1/DTM-C for ORR are 0.74 mA cm^{-2} and 286 mA mg^{-1} (at 0.9 V vs. RHE), which are 2.5 and 3.0 times higher

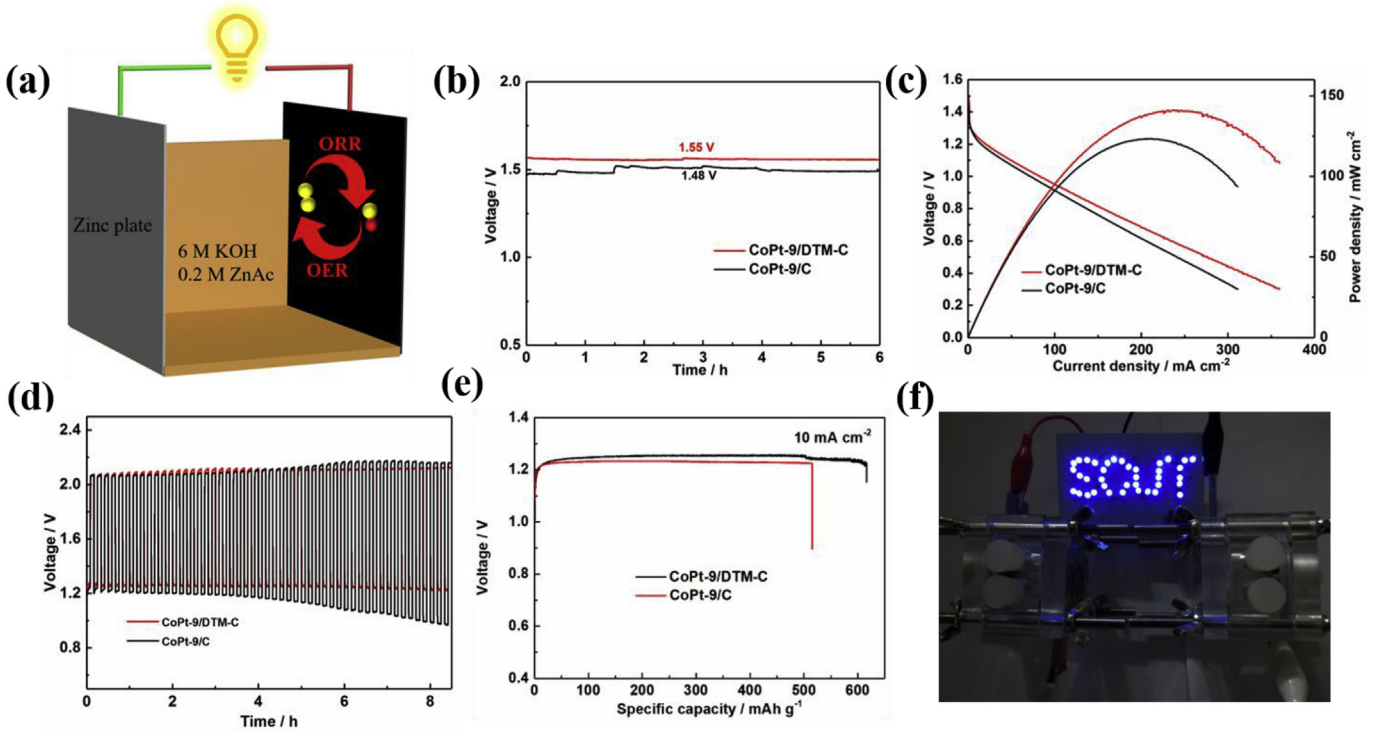

Fig. 7. (a) Schematic representation of the rechargeable Zn-air battery. (b) Open-circuit potential plots. (c) Discharge polarization and the corresponding power density curves. (d) Galvanostatic discharge–charge cycling curves at 2 mA cm^{-2}. (e) Galvanostatic discharge specific capacity curves at 10 mA cm^{-2}. (f) Photograph of a blue LED (≈3.0 V) powered by two liquid Zn-air batteries with the CoPt-9/DTM-C air-cathode connected in series. (For interpretation of the references to colour in this figure legend, the reader is referred to the Web version of this article.)

than that of CoPt-1/C catalyst; For OER, the overpotential of CoPt-9/DTM-C decreases nearly 30 mV at 10 mA cm^{-2}, the Tafel slope also reduces 16 mV dec^{-1} and the durability enhances 10% versus CoPt-9/C catalyst. Finally, these nanocomposite catalysts as air-cathode of self-assembled rechargeable Zn-air battery were tested. The presence of DTM boosted the performance of CoPt nanoparticles with a high open circuit potential, excellent discharging power density, desirable discharging specific capacity and long steady cycling life. The findings here may pave a pathway for designing cost-effective bifunctional electrocatalysts for Zn-air batteries, and introduction of DTM to other systems to further interrogate the universality of this strategy is currently underway in our lab.

Acknowledgements

Z. H. T. thanks financial support from National Natural Science Foundation of China (21501059), Guangdong Innovative and Entrepreneurial Research Team Program (No. 2014ZT05N200), Guangdong Natural Science Funds for Distinguished Young Scholars (No. 2015A030306006) as well as the Science and Technology Program of Guangdong Province (No. 2017A050506014).

Appendix A. Supplementary data

Supplementary data related to this article can be found at https://doi.org/10.1016/j.electacta.2018.07.154.

References

[1] Y. Li, H. Dai, Recent advances in zinc-air batteries, Chem. Soc. Rev. 43 (2014) 5257–5275.
[2] S. Hu, T. Han, C. Lin, W. Xiang, Y. Zhao, P. Gao, F. Du, X. Li, Y. Sun, Enhanced electrocatalysis via 3D graphene aerogel engineered with a silver nanowire network for ultrahigh-rate zinc–air batteries, Adv. Funct. Mater. 27 (2017), 1700041.
[3] J. Yin, Y. Li, F. Lv, Q. Fan, Y.-Q. Zhao, Q. Zhang, W. Wang, F. Cheng, P. Xi, S. Guo, NiO/con porous nanowires as efficient bifunctional catalysts for Zn–Air batteries, ACS Nano 11 (2017) 2275–2283.
[4] M. Liu, R. Zhang, W. Chen, Graphene-supported nanoelectrocatalysts for fuel cells: synthesis, properties, and applications, Chem. Rev. 114 (2014) 5117–5160.
[5] P. Strasser, Free electrons to molecular bonds and back: closing the energetic oxygen reduction (ORR)–Oxygen evolution (OER) cycle using core–shell nanoelectrocatalysts, Acc. Chem. Res. 49 (2016) 2658–2668.
[6] Q. Zhao, Z. Yan, C. Chen, J. Chen, Spinels: controlled preparation, oxygen reduction/evolution reaction application, and beyond, Chem. Rev. 117 (2017) 10121–10211.
[7] D. Yan, Y. Li, J. Huo, R. Chen, L. Dai, S. Wang, Defect chemistry of nonprecious-metal electrocatalysts for oxygen reactions, Adv. Mater. (2017), 1606459.
[8] D.U. Lee, P. Xu, Z.P. Cano, A.G. Kashkooli, M.G. Park, Z. Chen, Recent progress and perspectives on bi-functional oxygen electrocatalysts for advanced rechargeable metal-air batteries, J. Mater. Chem. A 4 (2016) 7107–7134.
[9] Z.-L. Wang, D. Xu, J.-J. Xu, X.-B. Zhang, Oxygen electrocatalysts in metal-air batteries: from aqueous to nonaqueous electrolytes, Chem. Soc. Rev. 43 (2014) 7746–7786.
[10] L. An, Y. Li, M. Luo, J. Yin, Y.-Q. Zhao, C. Xu, F. Cheng, Y. Yang, P. Xi, S. Guo, Atomic-level coupled interfaces and lattice distortion on CuS/NiS2 nanocrystals boost oxygen catalysis for flexible Zn-Air batteries, Adv. Funct. Mater. (2017), 1703779.
[11] W. Wang, B. Lei, S. Guo, Engineering multimetallic nanocrystals for highly efficient oxygen reduction catalysts, Adv. Energy Mater. 6 (2016), 1600236.
[12] M. Shao, Q. Chang, J.-P. Dodelet, R. Chenitz, Recent advances in electrocatalysts for oxygen reduction reaction, Chem. Rev. 116 (2016) 3594–3657.
[13] L.C. Seitz, C.F. Dickens, K. Nishio, Y. Hikita, J. Montoya, A. Doyle, C. Kirk, A. Vojvodic, H.Y. Hwang, J.K. Norskov, T.F. Jaramillo, A highly active and stable $IrO_x/SrIrO_3$ catalyst for the oxygen evolution reaction, Science 353 (2016) 1011–1014.
[14] C. Wang, N.M. Markovic, V.R. Stamenkovic, Advanced platinum alloy electrocatalysts for the oxygen reduction reaction, ACS Catal. 2 (2012) 891–898.
[15] S. Guo, S. Zhang, D. Su, S. Sun, Seed-mediated synthesis of core/shell FePtM/FePt (M = Pd, Au) nanowires and their electrocatalysis for oxygen reduction reaction, J. Am. Chem. Soc. 135 (2013) 13879–13884.
[16] D.Y. Chung, S.W. Jun, G. Yoon, S.G. Kwon, D.Y. Shin, P. Seo, J.M. Yoo, H. Shin, Y.-H. Chung, H. Kim, B.S. Mun, K.-S. Lee, N.-S. Lee, S.J. Yoo, D.-H. Lim, K. Kang, Y.-E. Sung, T. Hyeon, Highly durable and active PtFe nanocatalyst for

electrochemical oxygen reduction reaction, J. Am. Chem. Soc. 137 (2015) 15478–15485.
[17] L. Bu, S. Guo, X. Zhang, X. Shen, D. Su, G. Lu, X. Zhu, J. Yao, J. Guo, X. Huang, Surface engineering of hierarchical platinum-cobalt nanowires for efficient electrocatalysis, Nat. Commun. 7 (2016) 11850.
[18] L. Wang, Z. Tang, W. Yan, Q. Wang, H. Yang, S. Chen, Co@Pt Core@Shell nanoparticles encapsulated in porous carbon derived from zeolitic imidazolate framework 67 for oxygen electroreduction in alkaline media, J. Power Sources 343 (2017) 458–466.
[19] V.R. Stamenkovic, B. Fowler, B.S. Mun, G. Wang, P.N. Ross, C.A. Lucas, N.M. Marković, Improved oxygen reduction activity on Pt3Ni(111) via increased surface site availability, Science 315 (2007) 493–497.
[20] X. Huang, Z. Zhao, L. Cao, Y. Chen, E. Zhu, Z. Lin, M. Li, A. Yan, A. Zettl, Y.M. Wang, X. Duan, T. Mueller, Y. Huang, High-performance transition metal–doped Pt_3Ni octahedra for oxygen reduction reaction, Science 348 (2015) 1230–1234.
[21] H. Jin, J. Wang, D. Su, Z. Wei, Z. Pang, Y. Wang, In situ cobalt–cobalt oxide/N-doped carbon hybrids as superior bifunctional electrocatalysts for hydrogen and oxygen evolution, J. Am. Chem. Soc. 137 (2015) 2688–2694.
[22] L. Xu, Q. Jiang, Z. Xiao, X. Li, J. Huo, S. Wang, L. Dai, Plasma-engraved Co_3O_4 nanosheets with oxygen vacancies and high surface area for the oxygen evolution reaction, Angew. Chem. Int. Ed. 55 (2016) 5277–5281.
[23] C.G. Morales-Guio, L. Liardet, X. Hu, Oxidatively electrodeposited thin-film transition metal (Oxy)hydroxides as oxygen evolution catalysts, J. Am. Chem. Soc. 138 (2016) 8946–8957.
[24] A. Grimaud, O. Diaz-Morales, B. Han, W.T. Hong, Y.-L. Lee, L. Giordano, K.A. Stoerzinger, M.T.M. Koper, Y. Shao-Horn, Activating lattice oxygen redox reactions in metal oxides to catalyse oxygen evolution, Nat. Chem. 9 (2017) 457–465.
[25] Z. Lu, G. Chen, Y. Li, H. Wang, J. Xie, L. Liao, C. Liu, Y. Liu, T. Wu, Y. Li, A.C. Luntz, M. Bajdich, Y. Cui, Identifying the active surfaces of electrochemically tuned LiCoO2 for oxygen evolution reaction, J. Am. Chem. Soc. 139 (2017) 6270–6276.
[26] X. Li, Q. Jiang, S. Dou, L. Deng, J. Huo, S. Wang, ZIF-67-derived Co-NC@CoP-NC nanopolyhedra as an efficient bifunctional oxygen electrocatalyst, J. Mater. Chem. A 4 (2016) 15836–15840.
[27] M. Kuang, G. Zheng, Nanostructured bifunctional redox electrocatalysts, Small 12 (2016) 5656–5675.
[28] S. Hu, G. Goenaga, C. Melton, T.A. Zawodzinski, D. Mukherjee, PtCo/CoOx nanocomposites: bifunctional electrocatalysts for oxygen reduction and evolution reactions synthesized via tandem laser ablation synthesis in solution-galvanic replacement reactions, Appl. Catal. B Environ. 182 (2016) 286–296.
[29] Z. Cui, Y. Li, G. Fu, X. Li, J.B. Goodenough, Robust Fe3Mo3C supported IrMn clusters as highly efficient bifunctional air electrode for metal–air battery, Adv. Mater. (2017) 1702385.
[30] Z. Cui, G. Fu, Y. Li, J.B. Goodenough, Ni_3FeN-Supported Fe3Pt intermetallic nanoalloy as a high-performance bifunctional catalyst for metal–air batteries, Angew. Chem. Int. Ed. 56 (2017) 9901–9905.
[31] L. Deng, D. Liu, P. Du, H. Bu, Y. Song, Q. Tian, W. Yuan, P. Yuan, Z. Liu, H. He, Enhancement of diatomite solid acidity by Al incorporation, as evaluated by the catalytic effects on the thermal decomposition of 12-aminolauric acid, Colloids Surf. A. Physicochem. Eng. Asp. 509 (2016) 190–194.
[32] P. Lv, C. Liu, Z. Rao, Review on clay mineral-based form-stable phase change materials: preparation, characterization and applications, Renew. Sustain. Energy Rev. 68 (2017) 707–726.
[33] T. Qian, J. Li, X. Min, W. Guan, Y. Deng, L. Ning, Enhanced thermal conductivity of PEG/diatomite shape-stabilized phase change materials with Ag nanoparticles for thermal energy storage, J. Mater. Chem. A 3 (2015) 8526–8536.
[34] S.-I. Choi, S.-U. Lee, W.Y. Kim, R. Choi, K. Hong, K.M. Nam, S.W. Han, J.T. Park, Composition-Controlled PtCo alloy nanocubes with tuned electrocatalytic activity for oxygen reduction, ACS Appl. Mater. Interfaces 4 (2012) 6228–6234.
[35] P. Wu, H. Zhang, Y. Qian, Y. Hu, H. Zhang, C. Cai, Composition- and aspect-ratio-dependent electrocatalytic performances of one-dimensional aligned Pt–Ni nanostructures, J. Phys. Chem. C 117 (2013) 19091–19100.
[36] Y. Zhao, J. Liu, Y. Zhao, F. Wang, Y. Song, Pt-Co secondary solid solution nanocrystals supported on carbon as next-generation catalysts for the oxygen reduction reaction, J. Mater. Chem. A 3 (2015) 20086–20091.
[37] J. Kitchin, J.K. Nørskov, M. Barteau, J. Chen, Modification of the surface electronic and chemical properties of Pt (111) by subsurface 3d transition metals, J. Chem. Phys. 120 (2004) 10240–10246.
[38] B. Hammer, J.K. Nørskov, Theoretical surface science and catalysis—calculations and concepts, Adv. Catal. 45 (2000) 71–129.
[39] B. Hammer, Y. Morikawa, J.K. Nørskov, CO chemisorption at metal surfaces and overlayers, Phys. Rev. Lett. 76 (1996) 2141.
[40] A. Ruban, B. Hammer, P. Stoltze, H.L. Skriver, J.K. Nørskov, Surface electronic structure and reactivity of transition and noble metals, J. Mol. Catal. Chem. 115 (1997) 421–429.
[41] K. Zhang, Q. Yue, G. Chen, Y. Zhai, L. Wang, H. Wang, J. Zhao, J. Liu, J. Jia, H. Li, Effects of acid treatment of Pt– Ni alloy nanoparticles@ graphene on the kinetics of the oxygen reduction reaction in acidic and alkaline solutions, J. Phys. Chem. C 115 (2010) 379–389.
[42] C.-H. Cui, S.-H. Yu, Engineering interface and surface of noble metal nanoparticle nanotubes toward enhanced catalytic activity for fuel cell applications, Acc. Chem. Res. 46 (2013) 1427–1437.
[43] G. He, Y. Song, K. Liu, A. Walter, S. Chen, S. Chen, Oxygen reduction catalyzed by platinum nanoparticles supported on graphene quantum dots, ACS Catal. 3 (2013) 831–838.
[44] L. Wang, Z. Tang, W. Yan, H. Yang, Q. Wang, S. Chen, Porous carbon-supported gold nanoparticles for oxygen reduction reaction: effects of nanoparticle size, ACS Appl. Mater. Interfaces 8 (2016) 20635–20641.
[45] Q. He, S. Mukerjee, Electrocatalysis of oxygen reduction on carbon-supported PtCo catalysts prepared by water-in-oil micro-emulsion, Electrochim. Acta 55 (2010) 1709–1719.
[46] Y. Zhao, J. Liu, Y. Zhao, F. Wang, Composition-controlled synthesis of carbon-supported Pt–Co alloy nanoparticles and the origin of their ORR activity enhancement, Phys. Chem. Chem. Phys. 16 (2014) 19298–19306.
[47] J.-G. Oh, H.-S. Oh, W.H. Lee, H. Kim, Preparation of carbon-supported nano-segregated Pt alloy catalysts for the oxygen reduction reaction using a silica encapsulation process to inhibit the sintering effect during heat treatment, J. Mater. Chem. 22 (2012) 15215–15220.
[48] P. Roy, R. Ravindranath, A.P. Periasamy, C.-W. Lien, C.-T. Liang, H.-T. Chang, Green synthesis of Si-GQD nanocomposites as cost-effective catalysts for oxygen reduction reaction, RSC Adv. 6 (2016) 108941–108947.
[49] S. Takenaka, H. Matsumori, K. Nakagawa, H. Matsune, E. Tanabe, M. Kishida, Improvement in the durability of Pt electrocatalysts by coverage with silica layers, J. Phys. Chem. C 111 (2007) 15133–15136.
[50] S. Takenaka, H. Miyamoto, Y. Utsunomiya, H. Matsune, M. Kishida, Catalytic activity of highly durable Pt/CNT catalysts covered with hydrophobic silica layers for the oxygen reduction reaction in PEFCs, J. Phys. Chem. C 118 (2014) 774–783.
[51] Y. Li, M. Gong, Y. Liang, J. Feng, J.-E. Kim, H. Wang, G. Hong, B. Zhang, H. Dai, Advanced zinc-air batteries based on high-performance hybrid electrocatalysts, Nat. Commun. 4 (2013) 1805.
[52] M. Yu, Z. Wang, C. Hou, Z. Wang, C. Liang, C. Zhao, Y. Tong, X. Lu, S. Yang, Nitrogen-Doped Co3O4 mesoporous nanowire arrays as an additive-free air-cathode for flexible solid-state zinc–air batteries, Adv. Mater. 29 (2017), 1602868.